



Effect of Ni interlayer on microstructures and mechanical properties of 2205 duplex stainless steel joint by laser oscillating welding

Jing-wei Yang¹ · Xu-yang Liu¹ · Tao Li¹ · Lai-cai Chen¹ · Kai Yang² · Zong-ye Ding^{1,3,4} · Jie Zhang⁵ · Jian Qiao¹

Received: 5 June 2024 / Revised: 24 June 2024 / Accepted: 29 June 2024
© China Iron and Steel Research Institute Group Co., Ltd. 2024

Abstract

Laser oscillating welding of 2205 duplex stainless steel was performed using Ni interlayer as filler material. The influence of stirring effect caused by laser oscillating and Ni addition in the behavior of molten pool and the microstructure evolution was investigated. The results shows that Ni addition decreased the ratio of chromium equivalent and nickel equivalent in the molten pool and accelerated the austenitic transformation. The austenite/ferrite ratio was regulated, and the precipitation of nitrides was suppressed in the weld seam. The stirring effect caused by the oscillating beam facilitated the uniform distribution of Ni elements within the molten pool, promoting the formation of the homogeneous microstructures in the weld seam. With increasing the thickness of Ni interlayer, both the dimension and the peak temperature of molten pool decrease, further increasing the cooling rate and refining the grain size. When the thickness of Ni interlayer was 50 μm , the austenite/ferrite ratio in the weld seam was close to 1:1, and the grain size reached the minimum value. The tensile strength and ductility of the welded joint using Ni interlayer with thickness were 774 MPa and 25%, respectively, significantly improving the mechanical properties of 2205 duplex stainless steel joint welded without Ni addition.

Keywords 2205 duplex stainless steel · Ni interlayer · Laser welding · Microstructure · Mechanical property

1 Introduction

Duplex stainless steel (DSS) has been widely used in chemical, petrochemical and marine engineering industries, mainly due to its excellent resistance to pitting and

stress corrosion cracking, high strength as well as its good toughness [1–4]. Welding is an important fabrication technology for manufacturing these components. Conventional low energy density arc welding, like gas tungsten arc welding (GTAW), is an attractive method for the preparation of DSS components due to its controlled heat input and stable process [5]. By optimizing welding parameters, the dual phase balance could be regulated. However, GTAW is also challenged by the increasing width of the heat-affected zone (HAZ), the increasing precipitates, like nitride Cr_2N and the carbide M_{23}C_6 , and the decreased toughness of HAZ. Additionally, the chromium-depleted areas within HAZ were formed, escalating the susceptibility to intergranular corrosion, particularly in chloride-rich environments. The risk of weld distortion is also heightened, compromising dimensional precision of the joint. Generally, the limited heat input corresponds to a lower welding speed, which can hinder the efficiency of GTAW. Moreover, the lower arc energy density restricts its use in welding medium-thickness plates [2].

Compared to conventional arc welding, power beam welding techniques, including plasma arc welding [6, 7], keyhole tungsten inert gas welding (K-TIG) [8], laser

✉ Zong-ye Ding
dingzongye@hotmail.com

✉ Jian Qiao
qiaoj@fosu.edu.cn

¹ School of Mechatronic Engineering and Automation, Foshan University, Foshan 528000, Guangdong, China

² Key Laboratory of Advanced Manufacturing Technology of the Ministry of Education, Guizhou University, Guiyang 550025, Guizhou, China

³ State Key Laboratory of Advanced Brazing Filler Metals & Technology, Zhengzhou Research Institute of Mechanical Engineering Co., Ltd., Zhengzhou 450001, Henan, China

⁴ China National United Engineering Laboratory for Advanced Bearing Tribology, Henan University of Science and Technology, Luoyang 471023, Henan, China

⁵ School of Mechanical Engineering, University of Science and Technology Beijing, Beijing 100083, China

welding [9] and electron beam welding (EBW) [7, 10], become more attractive methods because of their advantages of larger melting depth, narrower HAZ, smaller welding distortion and higher efficiency. Moreover, these techniques could effectively suppress the growth of δ grains within HAZ. However, because the higher solidification rate of molten pool during power beam welding, the ratio of austenite/ferrite (δ/γ) tends to be unbalanced in the weld, adversely affecting the performance of the joints. Consequently, research has focused on improving δ/γ phase ratio in high-energy beam welded DSS joints. Currently, research on enhancing δ/γ phase ratio in DSS welds mainly focuses on three aspects: post-weld heat treatment, optimizing weld thermal cycles and improving weld chemical composition. The effect of heat treatment process on the evolution of weld microstructure was investigated by Refs. [11–13]. The results suggested that appropriate post-weld heat treatment can significantly improve the microstructure and overall properties of DSS joints. Nonetheless, Yang et al. [14] noted that heat treatment can increase production costs and extend the manufacturing cycle, particularly for large or complex components. In terms of optimizing the thermal cycle of the weld, Krasnorutskiy et al. [15] applied multiple electron beams with varying power distributions to create multiple melt pools, effectively increasing the size of melt pool. This approach has been shown to significantly increase the cooling time and reduce the cooling rate of the molten pool, leading to a decrease in δ content and improved joint performance, compared to conventional EBW. Similarly, Zhang et al. [16] and Tan et al. [17] employed multi-pass welding technology to improve the thermal cycle, and the cooling time of molten pool was increased significantly. Compared with the above methods, using high-Ni filler materials is a direct method to improve weld microstructure, since the controlled Ni addition during welding is helpful to attain the desired phase balance [7]. Wu et al. [18] and Strasse et al. [19] have effectively improved γ/δ ratio in laser beam welding of 2205 DSS by introducing Ni powder. It was also reported that an optimal γ/δ ratio was achieved by EBW of thick 2205 DSS plates with Ni-based filler wires [4]. However, the current method of Ni addition is predominantly introduced from the top of the weld, leading to Ni accumulation in the upper regions and uneven mixing with the base metal. This inhomogeneity can affect γ/δ ratio throughout the weld depth and limits the improvement of mechanical properties [4, 18, 19]. Although Ni addition could increase Ni equivalent (Ni_{eq}), it tends to concentrate in the center of weld, posing a challenge for achieving a uniform distribution of Ni during welding. Therefore, further research is necessary to ensure the uniform distribution of Ni within the weld for a homogeneous microstructure.

In recent years, laser oscillating welding has emerged as a prominent research area because it could enhance heat exchange and promote the uniform distribution of elements within the molten pool, owing to the stirring and vortex effects induced by the oscillating keyhole [20–22]. Capitalizing on this, the current study presents laser oscillation butt welding experiments on 2205 DSS utilizing Ni interlayers as the filler material. The effect of Ni foil thickness on the molten pool morphology, thermal cycles, δ/γ ratios, grain structures and precipitates was investigated. The corresponding mechanical properties were also characterized. The aim of this work is broadening the applicability of laser oscillating welding techniques for DSS.

2 Experimental

Figure 1a shows schematic diagram of the experimental setup for laser oscillating welding. 2205 DSS plates were welded using an IPG YLR-2000 fiber laser with a maximum output power of 2 kW. The laser wavelength was set to 1070 nm, and the laser spot diameter was approximately 0.2 mm. IPG-D30 laser oscillating head was mounted on a Fanuc 6-axis robot. During welding, the scan head was driven by the robot to move linearly, while the laser beam was set perpendicular to the surfaces of the welded plates, as shown in Fig. 1a. A circular trajectory of beam oscillation was employed in experiments (Fig. 1a). The welding parameters are summarized in Table 1.

A 3.0-mm-thick 2205 DSS plate produced by Baowu was selected as the base metal (BM), which was machined to pieces with dimension of 15 cm \times 7.5 cm for the butt joint. The chemical composition of 2205 DSS is C 0.023, Si 0.44, Mn 1.15, Ni 5.15, Cr 22.27, Mo 3.09, N 0.16 and Fe balance (in wt.%). The thickness of Ni interlayer (NL) is 20, 50 and 100 μ m. As shown in Fig. 1b, Ni interlayer was placed between DSS plates to form different joints and compared with the case where no Ni addition was used.

A colorimetric two-color pyrometer (ISR 12-LO, 1.28/1.64 μ m wavelength) was employed to monitor the thermal cycle of the weld pool. The pyrometer was fixed on the welding head (Fig. 1a), and the acquisition spot size of each pyrometer was adjusted to 0.4 mm. The temperature information about the molten pool was recorded by Ni-USB-6366 data acquisition system, and the data was stored on a computer for subsequent data processing. The flow behavior of the molten pool was recorded by Phantom VOE710 high-speed camera with a frame rate of 4000 frames per second (fps). A high-frequency auxiliary illumination laser (Cavitar Cavilux Smart) with a wavelength of 640 nm was employed for the experiments, and the exposure time was 0.25 μ s.

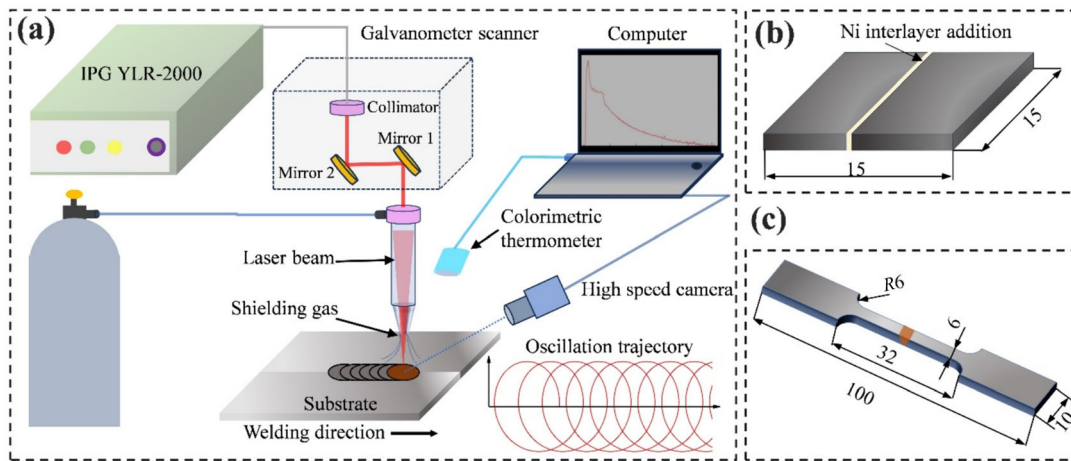


Fig. 1 Schematic diagram of experimental setup (a), welded sample geometry (b), and dimensions of tensile sample (c)

Table 1 Experimental parameters used in laser oscillating welding

Laser power/W	Welding speed/(cm min ⁻¹)	Oscillating pattern	Oscillating frequency/Hz	Oscillating diameter/mm
1500	75	Circular	100	1.2

The samples prepared for metallographic observations were cross-sectioned perpendicular to the welding direction. For revealing δ and γ phases, the samples were firstly grinded, polished and subsequently electrolytic etched applying a 30% sodium hydroxide solution for 60 s under electrolysis voltage of 3 V. And then, for further observing the precipitation of nitrides, another electrochemical etching with a 10% oxalic acid (3 V for 15 s) was also conducted on the samples. The microstructures were examined by optical microscopy (OM, Leica-DMi-8C) and scanning electron microscopy (SEM, JEOL-JSM7100F) equipped with an electron backscatter diffraction (EBSD, Channel 5 software) module.

The microhardness of each joint was determined using a Vickers hardness tester (HVM-G31ST) at the load of 1.96 N and holding time of 15 s on the middle of cross section of the joint. The mechanical properties of the joints at room temperature were evaluated by tensile tests. The geometry and dimensions of the test coupons are provided in Fig. 1c. An AGX-100kNXD testing system with a constant cross-head speed of 2.0 mm/min was used for the experiments. Three samples were tested for each welding condition. The local strain evolution of the joints was measured using a digital image correlation (DIC) system (XTDIC-CONST) during tensile tests.

3 Results and discussion

3.1 Weld morphology

Figure 2 shows the cross-sectional macrostructure of welds with varying thicknesses of Ni interlayers. The macrostructure exhibits the characteristic features of deep penetration welding, with a wider upper zone and a narrower bottom zone. The fusion zone (FZ) in all welds is uniformly formed without any significant defects. As shown in Fig. 2e and f, there is a noticeable trend of decreasing top and bottom widths of FZ with increasing Ni interlayer thickness. This suggests that the energy required to melt the base metal may decrease as the welding process parameters are established.

3.2 Characteristics of molten pool

Figure 3 shows the dynamic evolution of the molten pool in one oscillating cycle (10 ms) with varying Ni interlayer additions. Obviously, the molten pool in laser oscillation welding exhibits a shape resembling a water droplet along the welding direction, characterized by a quasi-circular shape at the front end and a quasi-triangular shape at the rear end. The front fullness of the molten pool is due to the effect of circular motion of the key hole, while the elongation of the rear is attributed to the Marangoni force [23]. This shape is primarily due to the gradual solidification of molten pool under the conductive heat from the base materials as the heat source advances, resulting in a triangular form. As shown in Fig. 4a, the length of the molten pool along the welding direction decreases with increasing Ni addition, minimizing at 7.2 mm for 100 μ m in thickness. This represents a reduction of over 15% compared to

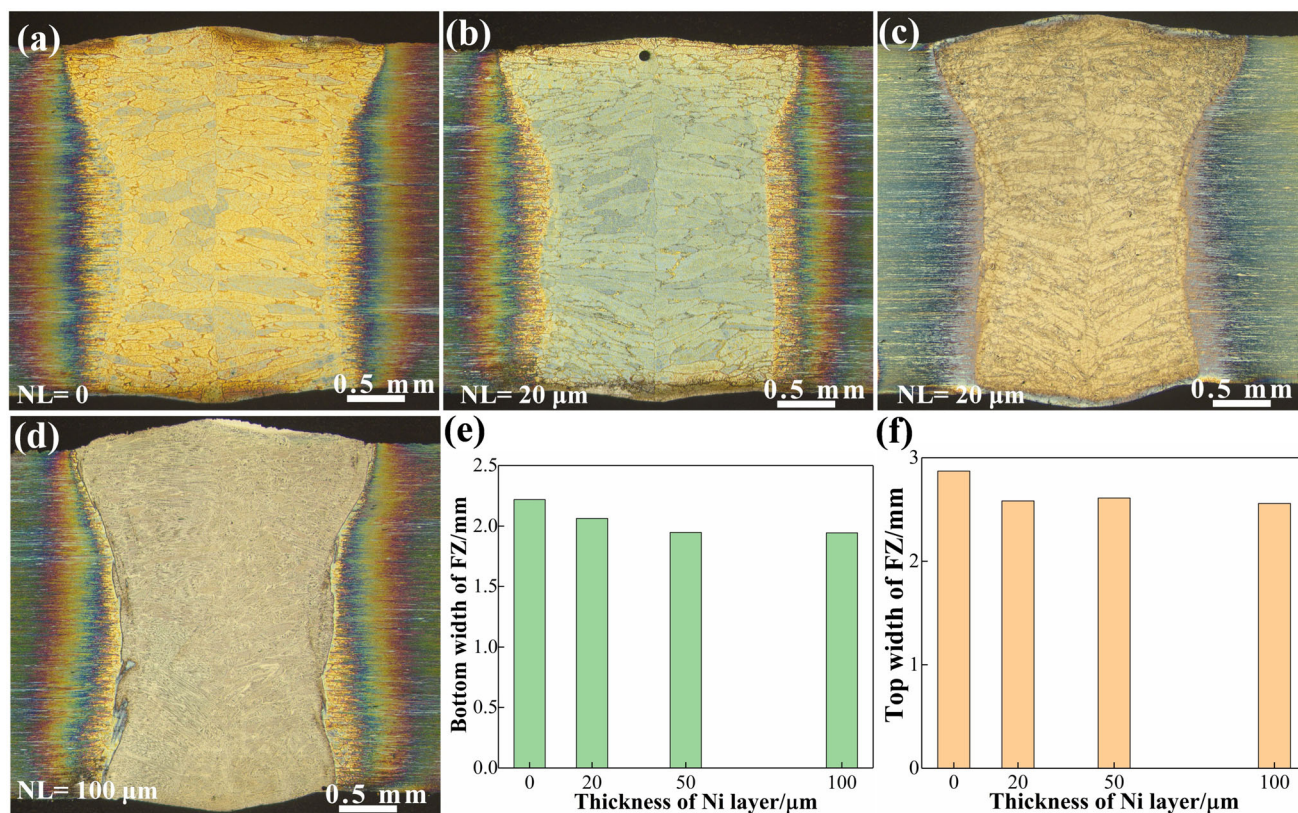


Fig. 2 Cross section and geometry parameters of welds with different Ni additions

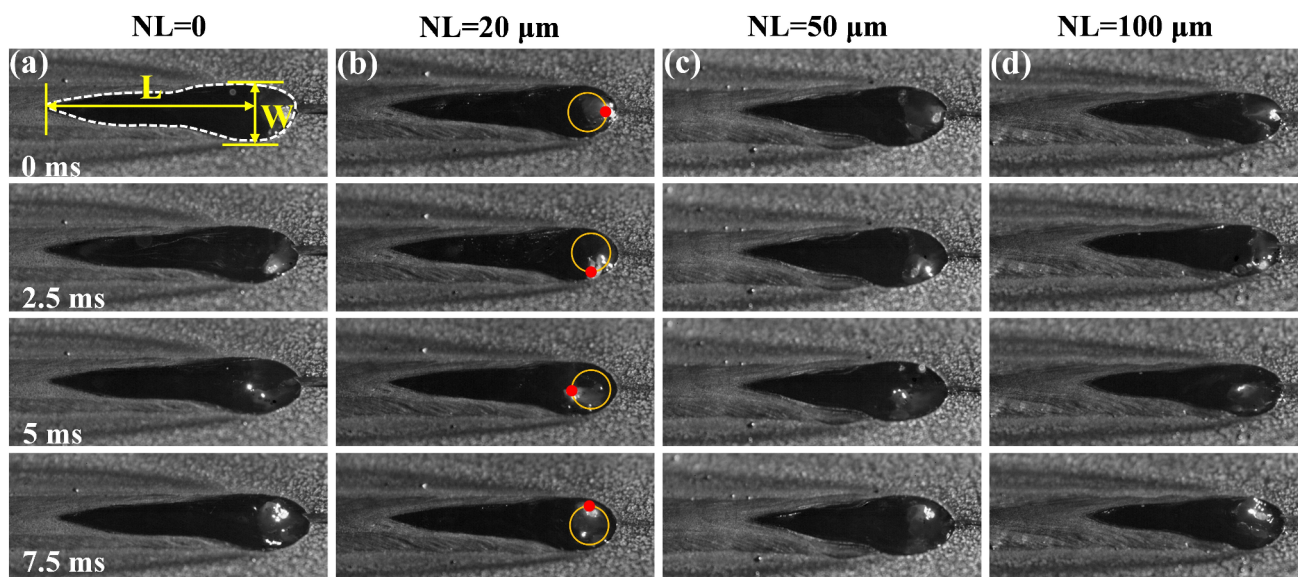


Fig. 3 Flow characteristics of molten pool with different Ni interlayers

welds without Ni addition. However, the width of the molten pool remains relatively unchanged, decreasing by only approximately 0.1 mm. This suggests that Ni addition can effectively reduce the size of molten pool.

The temperature of molten pool was measured and plotted against the welding time, as shown in Fig. 4b. As the thickness of Ni interlayer increases from 0 to 100 μm, the peak temperature drops from 2200 to approximately 1800 °C. This represents a reduction of about 20%

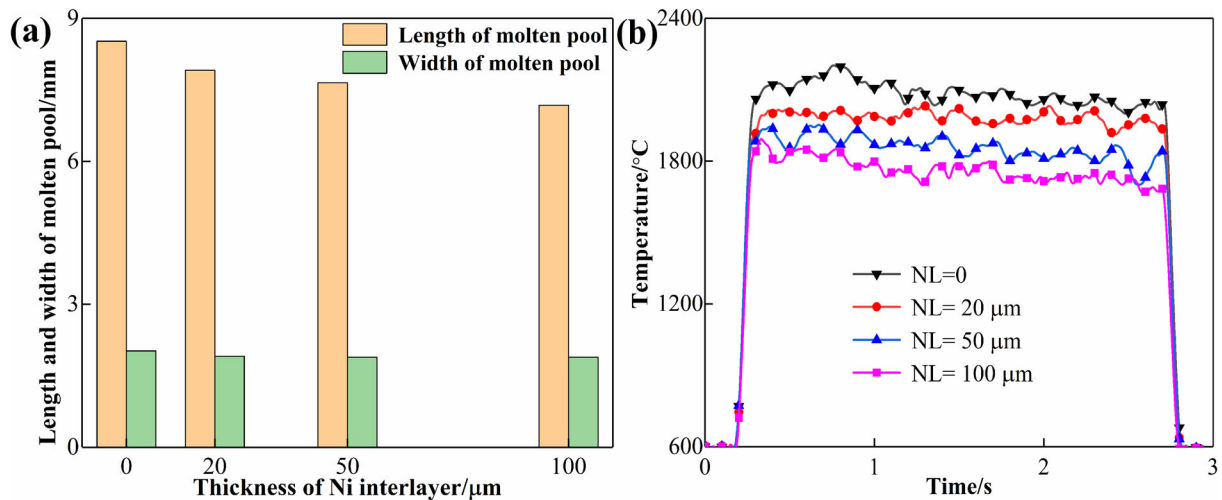


Fig. 4 Molten pool geometry sizes (a) and temperature cycle curves of molten pool (b) with different Ni interlayer additions

compared to weld without Ni addition, indicating a significant influence of Ni addition on the molten pool temperature.

Figure 5a illustrates the primary forces that propel fluid motion within the molten pool during laser welding, namely recoil pressure, vapor shear stress and surface tension. These forces are significantly influenced by temperature [21, 24]. Recoil pressure, resulting from metal vapor, varies inversely with the molten pool temperature, while surface tension at the pool center is reduced as temperature rises. As shown in Fig. 4b, the molten pool temperature decreases with Ni interlayer thickness. Consequently, the recoil pressure is reduced by the temperature drop, while surface tension paradoxically increases, causing a reduction in the tension gradient from the center to the edge of the molten pool. This reduction in gradient can attenuate the Marangoni convection effect. Furthermore, the density of the molten pool escalates with Ni addition, and a concurrent decline in temperature yields enhanced viscosity. This heightened viscosity engenders increased viscous resistance to metal flow. As a result, the diminished driving forces and increased flow resistance limit the

expansion of the molten pool, as depicted in Fig. 5b–e. This suggests that Ni addition influences the thermal behavior of the melt pool, which in turn affects the morphology and flow characteristics of the melt pool [25].

In addition to alterations in the size of molten pool, an asymmetrical morphology is also evident. As shown in Fig. 3, the molten pool exhibits a bias toward the right side of the welding direction. As reported in the previous references [23, 24], the circular trajectory during laser oscillating welding results in different instantaneous velocities on either side of the weld seam. This disparity causes slight variations in temperature and flow behavior across the molten pool, consequently forming an asymmetric morphology that contrasts with that of conventional laser welds.

3.3 Weld microstructure

3.3.1 Distribution and content of δ and γ phases

Figure 6 shows the microstructure of the welds across different regions from top to bottom. The microstructure,

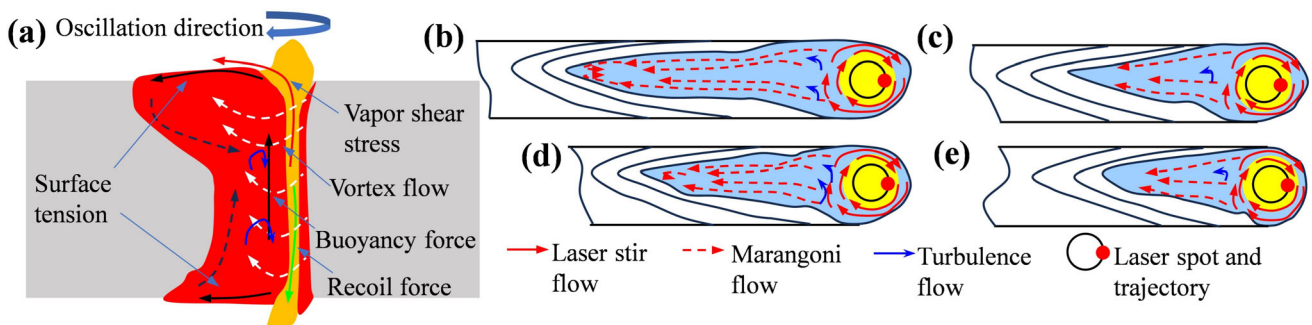


Fig. 5 Schematic diagram of driving forces in molten pool during laser oscillating welding (a) and melt flow with different Ni interlayers (b–e). b NL = 0; c NL = 20 μm ; d NL = 50 μm ; e NL = 100 μm

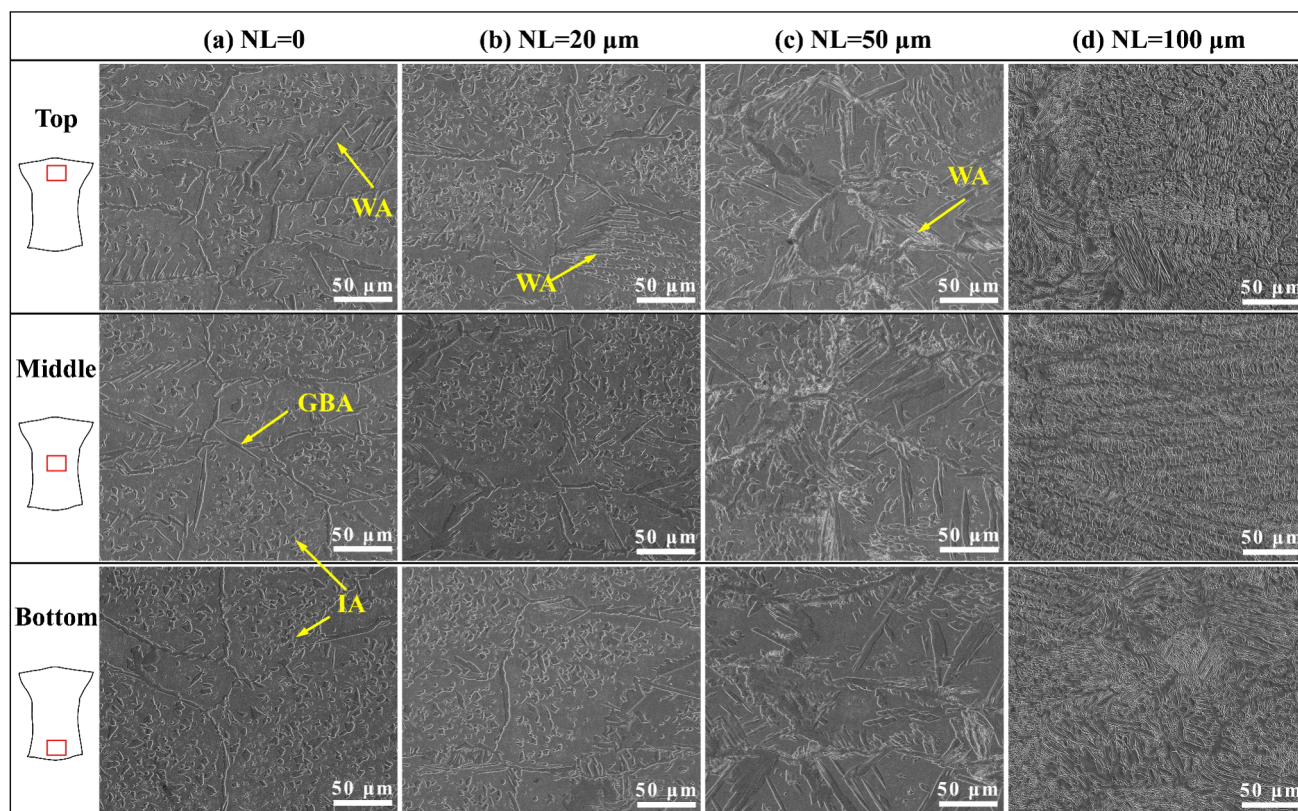


Fig. 6 Microstructures in top, middle and bottom regions of welds with different Ni additions

formed during the metallurgical process of laser oscillating welding, markedly differs from the ribbon-like structure of the base material in 2205 DSS. As reported by Leone and Kerr [26] that the weld metal solidifies following $\delta \rightarrow \gamma$ mode, indicating a transition from δ to γ phase as the molten pool cools from a high-temperature liquid phase. In DSS, γ phase typically forms through three mechanisms: grain boundary austenite (GBA) nucleating at the boundaries of δ grains, lath-like Widmanstätten austenite (WA) growing from grain boundaries into the grains and intragranular austenite (IA). As shown in Fig. 6a, IA and GBA are uniformly distributed throughout the weld without Ni addition. While a small amount of WA is observable in the upper and middle sections of the weld, there is a pronounced increase in IA in the lower section. Γ phase transformation in the weld is governed by both composition and cooling rate. GBA forms more readily at higher temperatures due to the enrichment of γ -stabilizing elements at grain boundaries, requiring less driving force. In contrast, IA formation necessitates greater undercooling, which is closely tied to the cooling rate. Without Ni addition, the material composition is consistent across the welding depth. During welding, laser energy coupling on the upper surface leads to heat accumulation in the surface

region of the weld, increasing the volume of molten metal in the upper and middle parts of the weld. This results in a slower cooling rate, conducive to WA growth in these areas. Conversely, in the lower part of the weld, the reduced volume of molten metal, as depicted in Fig. 3, leads to both increased cooling rates and undercooling. These conditions are advantageous for IA formation but detrimental to WA.

The microstructure in the weld seam significantly changed with Ni addition, as depicted in Figs. 6b–d. The increasing Ni content leads to a thickening of GBA and an increase in the volume of WA, which transitions from needle-like to flat-lobe-like structures, permeating the entire grain. Figure 7 shows γ phase content in the weld increases with Ni interlayer addition. At an Ni interlayer thickness of 50 μm , γ/δ ratio approaches equilibrium at approximately 1:1. Further increasing Ni addition to 100 μm results in a weld predominantly composed of coarse WA and GBA, as illustrated in Fig. 6d. Despite the decrease in the cooling rate with increased Ni content, IA gradually diminishes. This reduction in IA is attributed to the decreasing of chromium equivalent and nickel equivalent ($\text{Cr}_{\text{eq}}/\text{Ni}_{\text{eq}}$) ratio as Ni addition increases, shifting the weld solidification mode from $L \rightarrow L + \delta \rightarrow \delta \rightarrow \delta + \gamma$

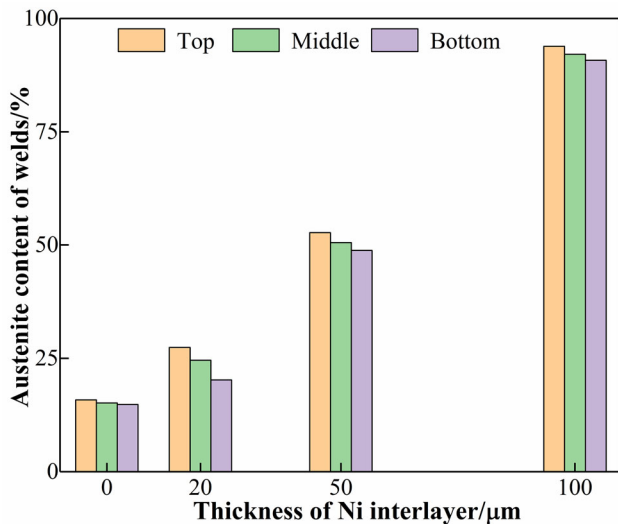


Fig. 7 Variation of γ content with different Ni additions

to $L \rightarrow L + \gamma + \delta \rightarrow \gamma$. Therefore, appropriate Ni addition during the welding of DSS aids in achieving a balanced two-phase microstructure. Figure 7 demonstrates that γ phase distribution across different weld locations is consistent, likely due to the stirring effect induced by the laser beam oscillation [22]. As shown in Fig. 5a, the circular oscillation of the keyhole modifies the melt flow, enhancing turbulence and promoting turbulent pumping within the melt pool. This action facilitates heat exchange and disperses Ni throughout the weld, enhancing the uniformity of γ phase distribution.

3.3.2 Grain size of δ and γ phases

Figure 8 shows the inverse pole figure images alongside the statistical distribution of δ and γ grain diameters in the welds with different Ni interlayer additions. The microstructure of δ is characterized by its typical strip-like columnar grains that grow directionally in accordance with the temperature gradient. In addition to the morphology of δ and γ phases (shown in Fig. 6), the grain size is also significantly influenced by Ni addition. As shown in Fig. 8, the average grain size of δ phase (δ_{avg}) decreased from 45 to 3.1 μm with increasing the thickness of Ni interlayer, while the average grain size of γ (γ_{avg}) increased from 3.2 to 10.2 μm . As a result, the disparity in grain size between δ and γ phases rapidly diminishes, and reaches a minimum of 2.2 μm at the thickness of 50 μm , a value nearly equivalent to that of the base metal. This indicates that an appropriate amount of Ni is thus instrumental in refining the grain size and minimizing disparity between γ and δ phases in the weld, which in turn, enhances the weld performance.

The final grain size is influenced by nucleation and growth processes. As shown in Figs. 3 and 4, both the size and temperature of the molten pool diminish with the addition of Ni, resulting in a more rapid cooling rate. This increased cooling rate is conducive to grain refinement, leading to a quick reduction in δ grain size within the weld. Conversely, the reduction of δ grains enhances the grain boundary area, providing additional nucleation sites for γ grains. Furthermore, the proliferation of γ grains restricts the growth of δ grains, contributing to their further refinement. Nevertheless, while a heightened cooling rate is advantageous for refining δ grains, it hinders the precipitation of γ phase. The findings in Fig. 4 suggest that the composition may be more critical in regulating phase equilibrium than the cooling rate. This is primarily because Ni addition not only shifts the thermodynamic equilibrium toward a higher γ phase fraction but also elevates $\gamma + \delta \rightarrow \gamma$ transformation line. Consequently, this allows γ precipitation to initiate at higher temperatures. The introduction of Ni disrupts the compositional balance of the molten pool, elevates the temperature of δ solid solution line and accelerates the phase transformation of δ phase. It is evident that by incorporating an Ni interlayer, an optimal balance can be readily achieved, and refined γ and δ grains can be obtained in laser welding.

3.3.3 Distribution of chromium nitrides

Figure 9 shows the distribution of nitride precipitation in welds with different Ni interlayer additions. Clearly, nitride precipitation predominantly occurs in HAZ and the lower region of the weld. This distribution is primarily associated with the rapid cooling rate, which could suppress $\delta \rightarrow \gamma$ phase transformation during the solidification. A detailed examination of HAZ characteristics, as shown in Fig. 10, reveals that both the width and grain size of HAZ decrease with the thickness of Ni interlayer. This is mainly attributed to the decreased temperature of the molten pool due to Ni addition, resulting in a lower peak temperature but a higher cooling rate in HAZ. Consequently, the growth of δ grains in HAZ is suppressed, and simultaneously, a greater amount of nitrogen precipitates within δ phase. Therefore, as Ni addition increases, the area of nitride precipitation is reduced, although the amount of precipitation within the grains does not change significantly, as shown in Fig. 9.

3.4 Mechanical properties

3.4.1 Microhardness

Figure 11 shows the microhardness distribution across the cross section of welds with different Ni additions. Clearly,

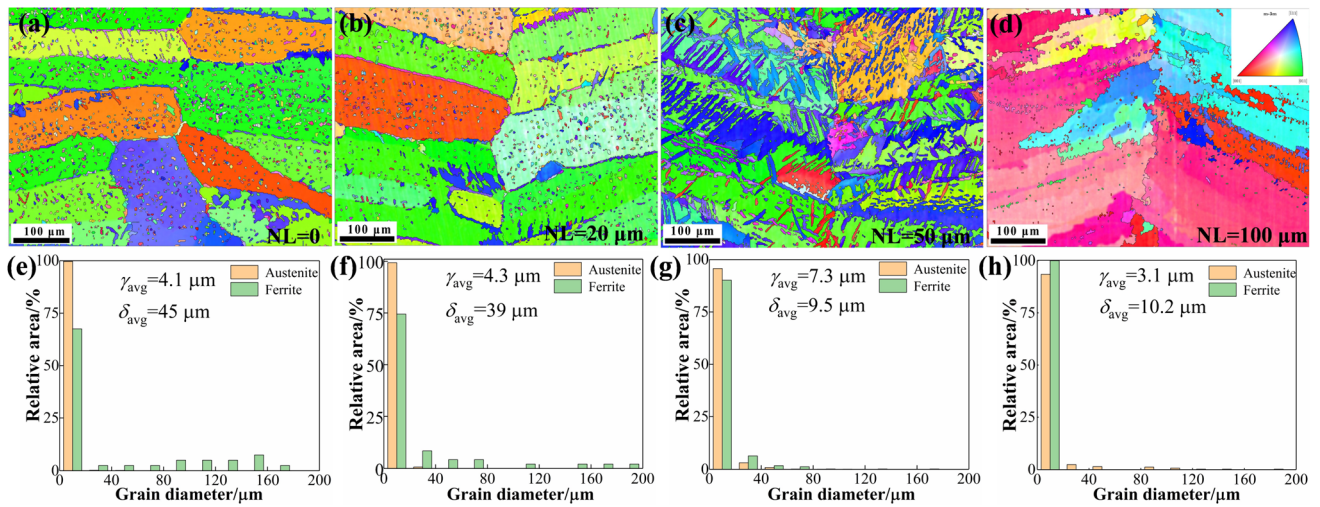


Fig. 8 EBSD orientation maps and grain size distribution with different Ni interlayers

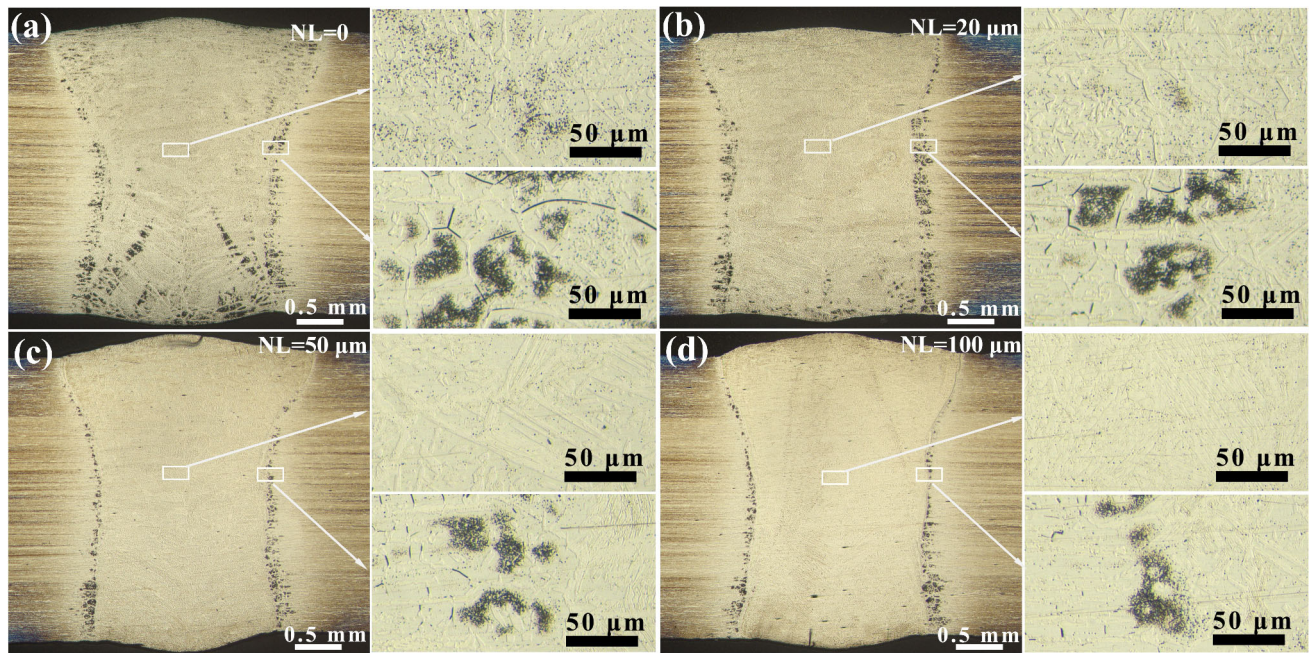


Fig. 9 Distribution of nitride precipitation with different Ni interlayers

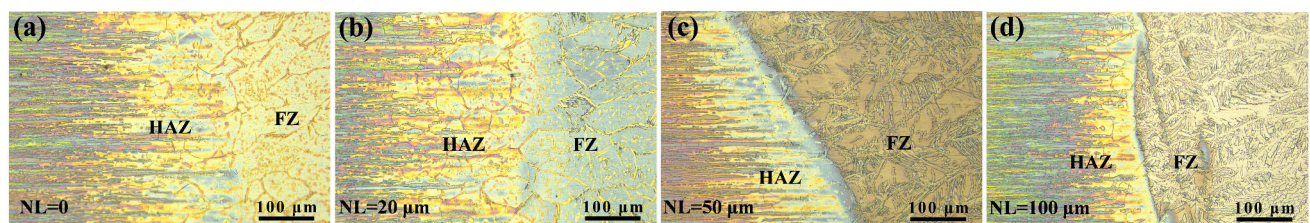


Fig. 10 Microstructural morphologies at HAZ with different Ni interlayers

there is a notable variation in the hardness distribution corresponding to different Ni additions. In the absence of Ni addition, the weld exhibits an average hardness of 289 HV, higher than that of the base metal. The hardness is reduced with the addition of Ni, and it further decreases as Ni content increases. Notably, at a Ni interlayer thickness of 50 μm , the hardness is nearly equivalent to that of the base metal. Additionally, the hardness profile, which exhibits a saddle shape, reveals significant variations in hardness across different regions of the weld.

It is widely recognized that the mechanical properties of welded joints are intrinsically related to the weld microstructure. In DSS welds, these properties are influenced by the solid solution, precipitation behavior, and the balance between γ and δ phases. Nitrogen is a strong solid solution strengthening element in DSS, and its solid solubility in γ phase is greater than that in δ phase. From Figs. 7 and 9, it can be seen that without Ni addition, the weld has a comparatively low γ content and a higher degree of nitride precipitation. This suggests that the contribution of solid solution strengthening from nitrogen is less significant than that of Ni addition. Nevertheless, the hardness curves depicted in Fig. 11 indicate that solid solution strengthening alone cannot account for the variation in hardness observed with different levels of Ni addition.

Thus, in terms of DSS, the effect of γ/δ ratio must be very significant on the hardness distribution. δ phase, influenced by alloying elements, typically exhibits a higher hardness than γ phase in DSS [27]. This suggests that a higher δ content could result in harder welds. While there is a scarcity of literature specifically addressing the effect of γ/δ ratio on the hardness of laser welded DSS joints,

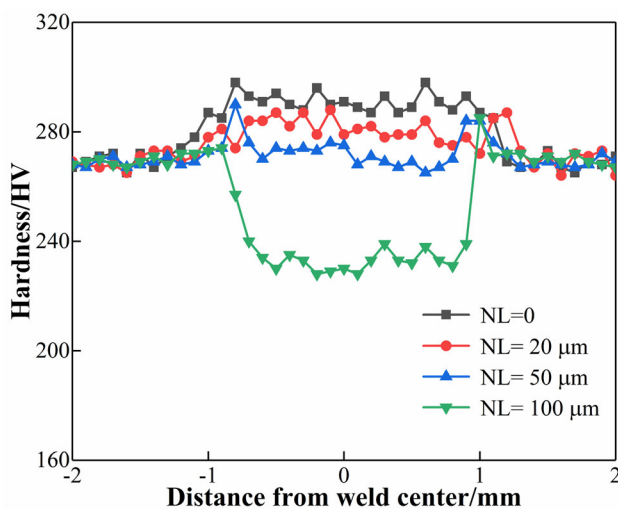


Fig. 11 Variation of microhardness with various Ni addition

studies on GTAW and EBW of DSS have reported an increase in weld hardness with δ content [5, 28], which corroborates our experimental findings. Furthermore, as noted by Kang and Lee [29], the presence of Cr_2N can impede dislocation motion and thus further increase the hardness weld. It is plausible to infer that in laser oscillation welding of DSS, γ/δ ratio and nitride precipitation are responsible for hardness variations. Consequently, the observation of peak hardness values in HAZ of the weld is not unexpected, given the elevated δ phase and chromium nitride content in HAZ (Fig. 9).

3.4.2 Tensile properties and DIC results

Figure 12a displays the stress–strain curves for laser oscillation welded joints with varying Ni additions. Clearly, both the tensile strength and elongation have been significantly improved by the addition of Ni. These properties increase with the thickness of Ni interlayer, and reach maximum values of tensile strength of 774 MPa and elongation of 25% at an interlayer thickness of 50 μm , and then decrease rapidly. This suggests that an optimal amount of Ni addition can effectively improve the performance of DSS welds. The fracture samples are shown in Fig. 12b–e. It can be seen that all the samples fractured at the weld seam excepted for the joint produced with Ni interlayer of 50 μm . This finding indicates that in laser welding of DSS, FZ is the most vulnerable part of the joint. It is different with the report by Mourad et al. [30] that almost all the laser welded joints failed in HAZ.

DIC technology was employed to capture the progression of local deformation and strain distribution throughout the tensile testing of the joints, as shown in Fig. 13. The stages of deformation, including encompassing elastic, plastic deformation, diffuse necking, local necking, and the initiation of failure, were examined to illustrate the strain distribution in joints with different Ni additions. Figure 13d–f presents the local axial strain along the gauge length at these stages. In the early stage of deformation (plastic deformation), the weld obtained at NL = 100 μm exhibits significantly greater local deformation compared to other joints, especially in the axial strain of the joint. This is particularly evident in the axial strain concentrated in FZ, aligning with the area of minimum hardness observed in Fig. 11. This phenomenon is predominantly due to the high γ content and reduced hardness resulting from an excessive Ni addition. As the tensile load increases to the diffusion necking stage, the strain concentration area for the joint without Ni addition is seen to transition from the base material to FZ, as shown in Fig. 13a. This migration underscores the pivotal role of microstructural

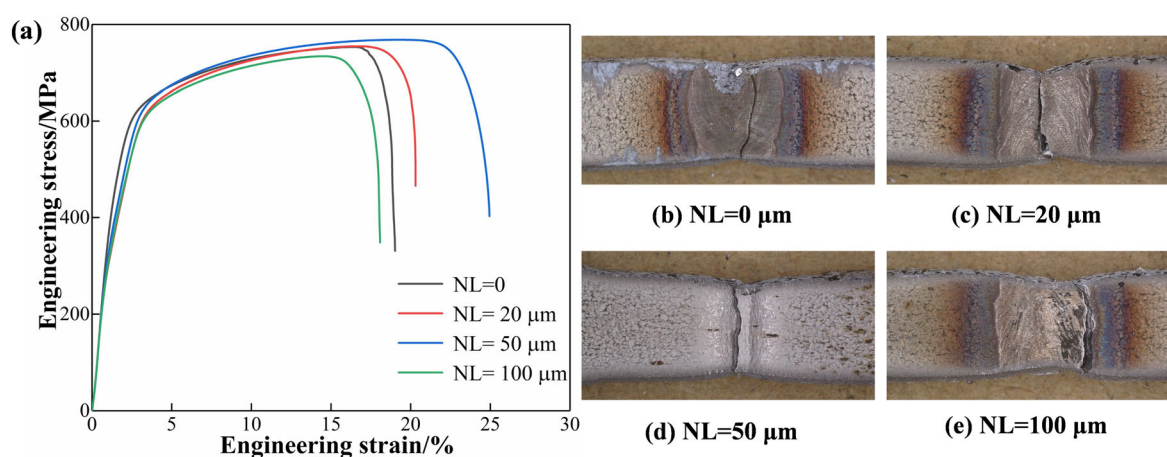


Fig. 12 Engineering stress–strain curves (a) and failure morphologies for joints produced with different Ni additions (b–e)

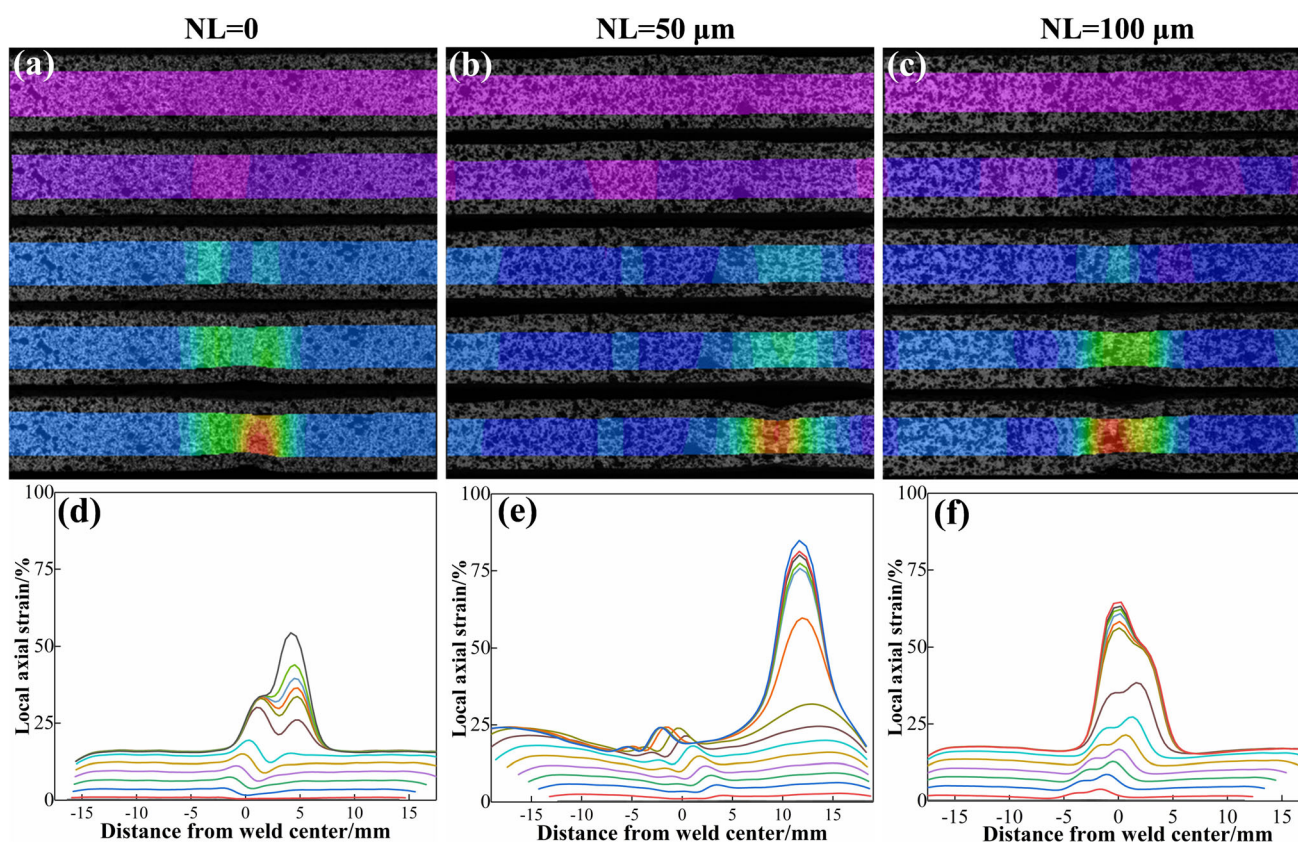


Fig. 13 Local strain maps at different deformation stages (a–c) and associated local axial strain profiles at various time (d–f)

balance in the weld evolution of local deformation and strain. Since deviation from an equilibrium two-phase structure can precipitate more detrimental phases [31]. In this study, an overabundance of δ phase leads to the formation of Cr_2N in the weld, as shown in Fig. 9. The accumulation of Cr_2N can induce stress concentration,

which facilitates the emergence of microcracks and the strain concentration in the weld area.

It is well accepted that γ/δ ratio in the weld substantially affects the mechanical properties of the joint. The addition of Ni is beneficial to maintaining a balanced two-phase structure within the weld. Additionally, the oscillation of

the laser beam facilitates the homogenization microstructure of FZ. Consequently, both the strength and ductility of the laser oscillating weld are enhanced with Ni addition. However, an overabundance of γ phase can be detrimental to joint performance, given that γ phase is less strong than δ phase in DSS [27]. In addition to γ/δ ratio, the effect of grain size on the joint performance must be considered. An increase in grain boundary area with a reduction in the average grain size of the weld can effectively impede dislocation movement during plastic deformation, thereby enhancing the mechanical properties of the joint. Furthermore, the disparity in grain size between γ and δ phases is minimized with Ni addition, reaching its lowest at an NL = 50 μm , as depicted in Fig. 8g. This promotes the generation of dislocations and encourages short-range interactions in distribution [32]. As a result, during tensile testing, BM undergoes plastic deformation preferentially, leading to concentrated deformation in BM area, as evidenced by DIC results in Fig. 13b. Ultimately, when deformation is substantial, cracks with significant diameter reduction are observed within BM, as illustrated in Fig. 12b, indicating that the joint strength surpasses that of BM.

4 Conclusions

1. Ni addition weakened the flow dynamics and thermal cycling within the molten pool. The increasing Ni content decreased the size and peak temperature of the molten pool. When the thickness of Ni interlayer was 100 μm , the length and peak temperature of molten pool decreased to 7.2 mm and 1800 $^{\circ}\text{C}$, respectively. Further, the cooling rate of the molten pool increased, promoting the grain refinement in the weld seam.
2. Ni addition decreased $\text{Cr}_{\text{eq}}/\text{Ni}_{\text{eq}}$ ratio, leading to the phase transition mode in the molten pool changing from $\text{L} \rightarrow \text{L} + \delta \rightarrow \delta \rightarrow \delta + \gamma$ to $\text{L} \rightarrow \text{L} + \gamma + \delta \rightarrow \gamma + \delta$ during cooling, which promoted the formation of γ and mitigated the precipitation of nitrides. The oscillation of laser beam generated a stirring effect facilitating the uniform dispersion of Ni within the molten pool, further contributing to a homogeneous microstructure in the weld seam.
3. The mechanical properties of the joints are determined by the proportion and grain size of γ and δ phases. When the thickness of Ni interlayer was 50 μm , γ/δ ratio was 1:1, and the tensile strength and ductility of the joint was 774 MPa and 25%, respectively, accompanied by the minimum grain size. In addition, the fracture occurred in BM.

Acknowledgements This work was financially supported by the National Natural Science Foundation of China (51805084 and 52265062), Project National United Engineering Laboratory for Advanced Bearing Tribology (202207) and Guangdong Basic and Applied Basic Research Foundation (2023B1515120086 and 2023A1515140124).

Declarations

Conflict of interest Zong-ye Ding is a youth editorial board member for *Journal of Iron and Steel Research International* and was not involved in the editorial review or the decision to publish this article. The authors declare no conflict of interest.

References

- [1] T.H. Wu, J.J. Wang, H.B. Li, Z.H. Jiang, C.M. Liu, H.Y. Zhang, *J. Iron Steel Res. Int.* 26 (2019) 435–441.
- [2] T. Tóth, S. Krasnorutskyi, J. Hensel, K. Dilger, *Int. J. Press. Vessels Pip.* 191 (2021) 104354.
- [3] Z.Q. Wei, X.R. Chen, H.G. Zhong, Q.J. Zhai, G. Wang, *J. Iron Steel Res. Int.* 24 (2017) 421–425.
- [4] J. Verma, R.V. Taiwade, *J. Manuf. Process.* 25 (2017) 134–152.
- [5] F. Li, Y. Liu, W. Ke, P. Jin, H. Kong, M. Chen, Q. Sun, *J. Manuf. Process.* 80 (2022) 581–590.
- [6] Q. Wang, G. Gu, C. Jia, K. Li, C. Wu, *J. Mater. Res. Technol.* 22 (2023) 355–374.
- [7] V. Muthupandi, P. Bala Srinivasan, S.K. Seshadri, S. Sundaresan, *Mater. Sci. Eng. A* 358 (2003) 9–16.
- [8] Z. Fei, Z. Pan, D. Cuiuri, H. Li, S. Van Duin, Z. Yu, *J. Manuf. Process.* 45 (2019) 340–355.
- [9] A.E. Odermatt, V. Ventzke, F. Dorn, R. Dinsé, P. Merhof, N. Kashaev, *J. Manuf. Process.* 72 (2021) 148–158.
- [10] K. Devendranath Ramkumar, D. Mishra, M.K. Vignesh, B. Ganesh Raj, N. Arivazhagan, S.V. Naren, S. Suresh Kumar, *J. Manuf. Process.* 16 (2014) 527–534.
- [11] M. Young, L. Tsay, C. Shin, S. Chan, *Int. J. Fatigue* 29 (2007) 2155–2162.
- [12] Z. Zhang, H. Jing, L. Xu, Y. Han, L. Zhao, X. Lv, J. Zhang, *J. Manuf. Process.* 31 (2018) 568–582.
- [13] J. Singh, A.S. Shahi, *J. Manuf. Process.* 50 (2020) 581–595.
- [14] Y. Yang, Z. Wang, H. Tan, J. Hong, Y. Jiang, L. Jiang, J. Li, *Corros. Sci.* 65 (2012) 472–480.
- [15] S. Krasnorutskyi, D. Keil, S. Schmigalla, M. Zinke, A. Heyn, H. Pries, *Weld. World* 56 (2012) 34–40.
- [16] Z. Zhang, H. Jing, L. Xu, Y. Han, L. Zhao, *Mater. Des.* 109 (2016) 670–685.
- [17] H. Tan, Z. Wang, Y. Jiang, Y. Yang, B. Deng, H. Song, J. Li, *Corros. Sci.* 55 (2012) 368–377.
- [18] H.C. Wu, L.W. Tsay, C. Chen, *ISIJ Int.* 44 (2004) 1720–1726.
- [19] A. Strasse, A. Gumenyuk, M. Rethmeier, in: *Lasers in Manufacturing Conference*, Munich, Germany, 2019, pp. 1–6.
- [20] H.H. Min, Q. Sun, Y.J. Xing, H.L. Liu, Y. Chen, X.N. Wang, L.N. Sun, *J. Iron Steel Res. Int.* (2023) <https://doi.org/10.1007/s42243-023-01087-0>.
- [21] C. Chen, Y. Xiang, M. Gao, *J. Manuf. Process.* 60 (2020) 180–187.
- [22] L. Wang, M. Gao, Z. Hao, *Int. J. Heat Mass Transf.* 151 (2020) 119467.
- [23] S. Yan, Z. Meng, B. Chen, C. Tan, X. Song, G. Wang, *Sci. Technol. Weld. Join.* 28 (2023) 173–181.
- [24] C. Chen, H. Zhou, C. Wang, L. Liu, Y. Zhang, K. Zhang, *J. Manuf. Process.* 68 (2021) 761–769.

- [25] L. Li, J. Gong, H. Xia, G. Peng, Y. Hao, S. Meng, J. Wang, J. Mater. Res. Technol. 11 (2021) 19–32.
- [26] G. Leone, H. Kerr, Weld. J. 61 (1982) 13s–22s.
- [27] M. Asif, M. K.A. Shrikrishna, P. Sathiya, J. Manuf. Process. 21 (2016) 196–200.
- [28] C.P. Meinhardt, M. Chludzinski, R.F. Ribeiro, C.L.F. Rocha, A.C.S. Santos, T.R. Strohaecker, J. Mater. Process. Technol. 246 (2017) 158–166.
- [29] D.H. Kang, H.W. Lee, Metall. Mater. Trans. A 43 (2012) 4678–4687.
- [30] A.H.I. Mourad, A. Khourshid, T. Sharef, Mater. Sci. Eng. A 549 (2012) 105–113.
- [31] V.S. Moura, L.D. Lima, J.M. Pardal, A.Y. Kina, R.R.A. Corte, S.S.M. Tavares, Mater. Charact. 59 (2008) 1127–1132.
- [32] X.F. Xie, J. Li, W. Jiang, Z. Dong, S.T. Tu, X. Zhai, X. Zhao, Mater. Sci. Eng. A 786 (2020) 139426.

Springer Nature or its licensor (e.g. a society or other partner) holds exclusive rights to this article under a publishing agreement with the author(s) or other rightsholder(s); author self-archiving of the accepted manuscript version of this article is solely governed by the terms of such publishing agreement and applicable law.